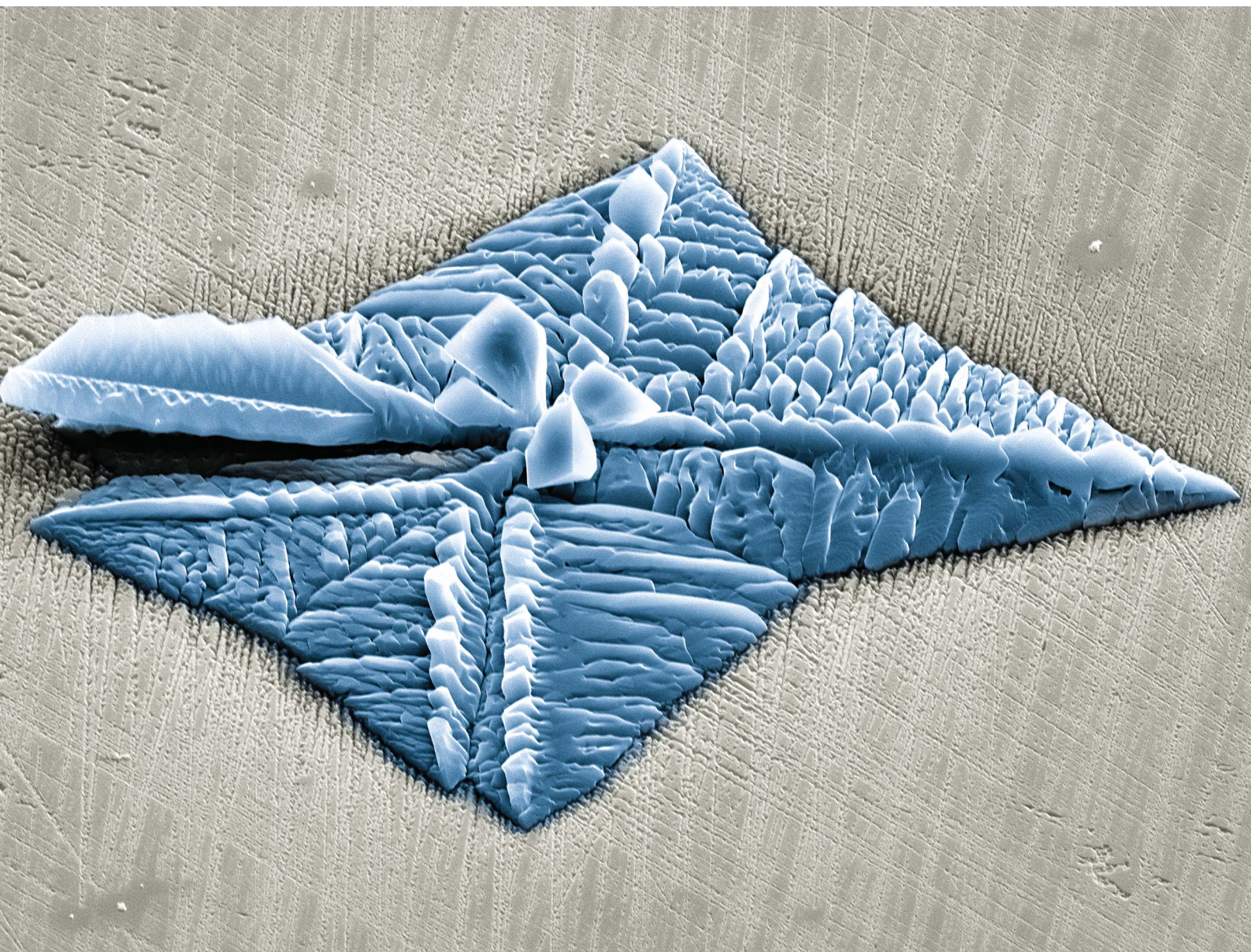


Journal of Materials Chemistry A

Materials for energy and sustainability

rsc.li/materials-a



ISSN 2050-7488

PAPER

Christoph. R. Müller *et al.*
Model structures of molten salt-promoted MgO to probe
the mechanism of MgCO_3 formation during CO_2 capture at a
solid-liquid interface

PAPER

[View Article Online](#)
[View Journal](#) | [View Issue](#)Cite this: *J. Mater. Chem. A*, 2022, 10, 16803Model structures of molten salt-promoted MgO to probe the mechanism of MgCO₃ formation during CO₂ capture at a solid–liquid interface†Alexander. H. Bork,^a Norbert Ackerl,^{ab} Joakim Reuteler,^c Sachin Jog,^a David Gut,^a Robert Zboray^d and Christoph. R. Müller^{ab*}

MgO is a promising solid oxide-based sorbent to capture anthropogenic CO₂ emissions due to its high theoretical gravimetric CO₂ uptake and its abundance. When MgO is coated with alkali metal salts such as LiNO₃, NaNO₃, KNO₃, or their mixtures, the kinetics of the CO₂ uptake reaction is significantly faster resulting in a 15 times higher CO₂ uptake compared to bare MgO. However, the underlying mechanism that leads to this dramatic increase in the carbonation rate is still unclear. This study aims to determine the most favourable location for the nucleation and growth of MgCO₃ and more specifically, whether the carbonation occurs preferentially at the buried interface, the triple phase boundary (TPB), and/or inside the molten salt of the NaNO₃–MgO system. For this purpose, a model system consisting of a MgO single crystal that is structured by ultra-short pulse laser ablation and coated with NaNO₃ as the promoter is used. To identify the location of nucleation and growth of MgCO₃, micro X-ray computed tomography, scanning electron microscopy, Raman microspectroscopy and optical profilometry were applied. We found that MgCO₃ forms at the NaNO₃/MgO interface and not inside the melt. Moreover, there was no preferential nucleation of MgCO₃ at the TPB when compared to the buried interface. Furthermore, it is found that there is no observable CO₂ diffusion limitation in the nucleation step. However, it was observed that CO₂ diffusion limits MgCO₃ crystal growth, *i.e.* the growth rate of MgCO₃ is approximately an order of magnitude faster in shallow grooves compared to that in deep grooves.

Received 11th April 2022

Accepted 8th July 2022

DOI: 10.1039/d2ta02897b

rsc.li/materials-a

Introduction

CO₂ absorption from large point sources such as power plants and its subsequent storage (carbon dioxide capture and storage, CCS) is a cost-effective approach to significantly reduce anthropogenic CO₂ emissions. Alkaline earth metal oxide-based sorbents that reversibly absorb and desorb CO₂ have attracted attention in the framework of CCS due to favourable cost estimates for CO₂ capture compared to amine scrubbing.^{1–3}

Magnesium oxide-based sorbents that capture CO₂ reversibly through the reaction $\text{MgO} + \text{CO}_2 \leftrightarrow \text{MgCO}_3$ at intermediate temperatures (300–500 °C) have shown great potential for CCS owing to its high theoretical gravimetric uptake (1.09 gCO₂ gMgO^{−1}) and low energy requirement for sorbent regeneration

(2.68 kJ g^{−1} CO₂) when compared to other metal oxide sorbents (*e.g.* 4.04 kJ g^{−1} CO₂ for CaO).^{4,5} However, bulk MgO exhibits sluggish carbonation kinetics resulting in low experimentally obtained uptakes of only 0.02 gCO₂ gMgO^{−1} after 1 hour of exposure to CO₂.^{4,5} To accelerate the kinetics of CO₂ uptake of MgO-based sorbents, different approaches, such as the increase of surface area, have been reported.^{4,6,7} However, the addition of alkali metal salts *e.g.* NaNO₃, KNO₃, LiNO₃ or mixtures thereof have resulted in the largest increases in the CO₂ uptake kinetics.^{8–11} It is important to notice, that an enhancement in the CO₂ uptake only occurs when the salt is in the molten state and for an optimized system containing 20 wt% NaNO₃ an CO₂ uptake of 0.31 gCO₂ gMgO^{−1} (after 60 min of carbonation) has been reported.^{9,10,12} Although there is consensus on the promoting effect of alkali metal salts, there is an ongoing debate on the mechanism(s) through which alkali metal salt promotes carbonate formation with accelerated rates.^{1,9,10,13–16} One hypothesis considers alkali metal salts (AMS) as phase transfer catalysts that dissolve MgO yielding solvated ionic [Mg²⁺...O^{2−}] pairs that have weaker bonds compared to the strong ionic bond of bulk MgO. According to density functional theory calculations by Zhang *et al.* the dissociation of MgO into a [Mg²⁺...O^{2−}] pair requires 7.1 eV (in vacuum) while only 5.3 eV is required in NaNO₃ due to solvation effects.⁹ In addition AMS

^aLaboratory of Energy Science and Engineering, Department of Mechanical and Process Engineering, ETH Zurich, CH-8092 Zürich, Switzerland. E-mail: muelchri@ethz.ch

^bNAPho – Norbert Ackerl Photonics, CH-8049 Zürich, Switzerland

^cScientific Center for Optical and Electron Microscopy, ETH Zurich, CH-8093 Zurich, Switzerland

^dCenter for X-ray Analytics, Empa, Swiss Federal Laboratories for Materials Science and Technology, CH-8600 Dübendorf, Switzerland

† Electronic supplementary information (ESI) available. See <https://doi.org/10.1039/d2ta02897b>

have the ability to dissolve CO_2 promoting further its reaction with solvated $[\text{Mg}^{2+} \dots \text{O}^{2-}]$ pairs.^{9,17} Besides the mechanism itself, currently also the location of MgCO_3 growth and the rate limiting step is under debate, *i.e.* the dissolution of MgO or the dissolution of CO_2 .^{1,9,10}

Kinetic analysis of CO_2 absorption on AMS promoted MgO using thermogravimetric analysis (TGA) has revealed that the formation of MgCO_3 is characterized by a nucleation and growth process.¹⁰ In such a process the nucleation and growth of magnesium carbonate would rely on the dissolution of MgO and CO_2 in the AMS leading to a supersaturated solution of a magnesium carbonate precursor (*e.g.* $[\text{Mg}^{2+} \dots \text{CO}_3^{2-}]$) yielding ultimately crystalline MgCO_3 . A recent study into the growth process of MgCO_3 has shown that MgCO_3 grows in the form of 2D crystals with a sector plate morphology at the interface of NaNO_3/MgO , providing further evidence for a nucleation and growth process in which MgCO_3 precipitates as crystals from a supersaturated solution.¹⁵ While there is a general agreement on the nucleation and growth process for MgCO_3 formation,^{14,16} the location at which MgCO_3 precipitates most favorably is still unclear. Conceptually, MgCO_3 can form within the molten salt, at the interface of the salt and MgO (NaNO_3/MgO), often referred to as the “buried interface” or at the triple phase boundary (TPB), *i.e.* the interface of NaNO_3/MgO that is exposed to the CO_2 atmosphere. Answering this question, will provide important sorbent design guidelines as to whether an effective sorbent shall have a high TPB length or a large NaNO_3/MgO interface area.

Previous work aiming to address this question have applied *in situ* TEM analysis on AMS promoted MgO nanoparticles and observed that MgCO_3 precipitates at the TPB.^{14,18} Somewhat contradictory, a study using a $\text{MgO}(100)$ single crystal coated completely with NaNO_3 revealed the formation of MgCO_3 in the absence of a TPB.¹⁶ In another example, *in situ* X-ray diffraction on a sample of $\text{MgO}(100)$ promoted with NaNO_3 that is dispersed on the surface, evidenced the formation of crystalline MgCO_3 at the NaNO_3/MgO interface.¹⁵ Moreover, *ex situ* microscopy analysis of the formed MgCO_3 indicate a favorable growth of MgCO_3 at the buried interface.¹⁵ The indication (importantly not a direct proof) of growth at the buried interface was based on the observation of a 2D hemispherical zone of etched dissolution pyramidal pits at the surface of $\text{MgO}(100)$ under and around the 2D MgCO_3 crystals. Since both NaNO_3 and CO_2 are required for both the formation of such etching pits in MgO and the subsequent growth of MgCO_3 , the growth of a crystal ought to occur at the buried interface as it is unlikely that a dynamically expanding TPB exists at the perimeter of the (growing) crystal.¹⁵ However, besides some structural advantages of the $\text{NaNO}_3\text{--MgO}(100)$ model system it has a key disadvantage in that the dispersed molten AMS is mobile on the surface under operating conditions making the determination of the location of the AMS/ MgCO_3 interface very difficult, if not impossible. Therefore, a clear answer to the question whether MgCO_3 forms favorably at the TPB or the buried interface is still missing. To provide an unequivocal answer to this question, a model system of MgO that confines the (molten) AMS to a fixed location is required. To this end we use laser micro

processing to manufacture model geometries in MgO .^{19,20} An ultra-short pulsed (USP) laser system with pulse durations below a picosecond was used to fabricate grooves of controlled (yet varying) depth ensuring that the molten AMS remains at a fixed location during operation while providing both a TPB and a buried interface. Such well-defined model structures are subsequently characterized by micro X-ray computed tomography (μCT), scanning electron microscopy (SEM), Raman spectroscopy and optical profilometry to identify the location and quantify the amount of MgCO_3 grown. Our experimental results show clearly that MgCO_3 grows equally favorably at the buried interface and TPB. Furthermore, by varying the depth of the grooves in MgO allows for an assessment of the effect of the CO_2 diffusion path length from the gas atmosphere to the reaction interface on the growth rate, showing a faster growth of MgCO_3 in the shallow grooves *i.e.* for shorter CO_2 diffusion path lengths.

Results and discussion

Fabrication of model $\text{NaNO}_3\text{--MgO}$ structures

The fabrication of the $\text{NaNO}_3\text{--MgO}$ model structure is illustrated in Fig. 1. We used ultra-short pulse (USP) laser ablation to microstructure $\text{MgO}(100)$ single crystals with grooves of fixed width and varying depths, which are subsequently filled with NaNO_3 , as shown in Fig. 1a (see also ESI Fig. S1† for illustration

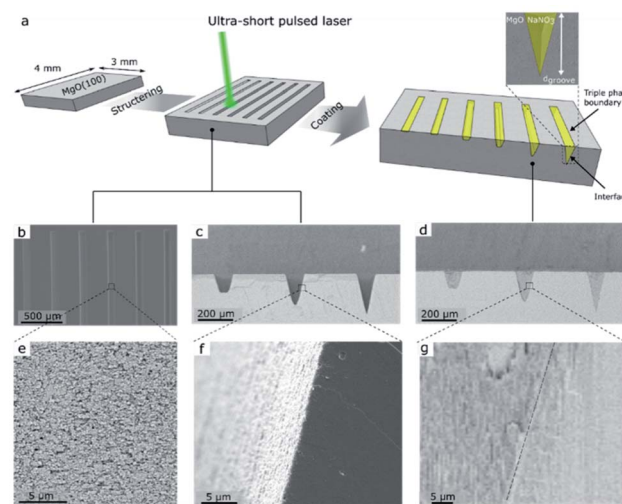


Fig. 1 Fabrication and SEM characterization of the $\text{NaNO}_3\text{--MgO}_A$ model structure to determine where MgCO_3 nucleates and grows most favorably during CO_2 capture. (a) Schematic of the fabrication process of the $\text{NaNO}_3\text{--MgO}_A$ model system using USP laser ablation to microstructure grooves in a $\text{MgO}(100)$ single crystal of depth, d_{groove} and top width w_{groove} , which are subsequently filled with NaNO_3 . The black arrows point to the triple phase boundary (TPB) line ($\text{CO}_2/\text{NaNO}_3/\text{MgO}$) and the (buried) NaNO_3/MgO interface. (b–g) SEM images of grooves without and with NaNO_3 . (b) Top view of six laser ablated grooves in a $\text{MgO}(100)$ single crystal. (c) Mechanically cleaved sample exposing cross-sections of three grooves without a NaNO_3 promoter and (d) shows the same three grooves with the NaNO_3 promoter. (e–g) high magnification images of the respective structures shown in (b–d).



of the USP laser setup and ablation process). Fig. 1 shows grooves of different depths, d_{groove} , and arrows point to the location of the (buried) NaNO_3/MgO interface and the triple phase boundary ($\text{CO}_2/\text{NaNO}_3/\text{MgO}$) line in such model sorbent structures. Two sets of MgO model grooves were fabricated and are referred here to as MgO_A and MgO_B . The sample MgO_A , shown in Fig. 1, was designed to contain grooves with a large difference between the most shallow ($d_{\text{groove}} = 5 \mu\text{m}$) and the deepest groove ($d_{\text{groove}} = 238 \mu\text{m}$) to explore also the effect of the diffusion length of CO_2 on the formation of MgCO_3 . Optical profilometry measurements rely on the reflection of incoming light. However, the steep walls of the groove in MgO_A limited reflection and consequently prevented the measurement of this sample by optical profilometry. Therefore, an additional sample referred to as MgO_B , with groove of depths between $d_{\text{groove}} = 6\text{--}180 \mu\text{m}$ was designed. The grooves had a wide and flat bottom to enable (top view) characterization of MgCO_3 formation by SEM and optical profilometry measurements (Fig. S2 and S3†). The shape and roughness of the microstructured grooves with and without NaNO_3 are visualized by SEM and are given in Fig. 1b–g). A top view of six grooves in MgO_A at different magnifications is shown in Fig. 1b and e, while cross-sections (with and without NaNO_3) are imaged in Fig. 1c–g. For MgO_A , all the grooves have the same length (and width of $3000 \mu\text{m}$ and $100 \mu\text{m}$ respectively, while the groove depths vary between $d_{\text{groove}} = 5\text{--}238 \mu\text{m}$. In sample MgO_B all grooves have an identical length ($3000 \mu\text{m}$) and the depths varied between $d_{\text{groove}} = 6\text{--}180 \mu\text{m}$. In addition, in sample MgO_B the width of the grooves was wider at the top ($200 \mu\text{m}$) and the grooves had a smaller taper angle than the ones in sample MgO_A allowing for a wide flat bottom to enable optical profilometry measurements as described earlier, Table S1.† The average roughness of the most shallow groove was *ca.* $0.41 \mu\text{m}$, and increased to *ca.* $1.1 \mu\text{m}$ for the deepest groove (ESI Fig. S3c†). Here, the average roughness is calculated as the standard deviation from the mean value along the length of the groove measured over a $600 \mu\text{m}$ wide window in the *y*-direction. A cross-sectional view of the alkali salt coated sample, *i.e.* $\text{NaNO}_3\text{--MgO_A}$, shows an intimate contact between the surface of MgO and the promoter NaNO_3 confirming an excellent wetting of the surface of MgO by NaNO_3 (Fig. 1g).

Carbonation and characterization of the $\text{NaNO}_3\text{--MgO}$ model system

The micro-structured, model $\text{NaNO}_3\text{--MgO}$ samples were exposed to typical CO_2 capture conditions of molten-salt promoted MgO .^{9,10,21} To this end, the as-prepared $\text{NaNO}_3\text{--MgO_A}$ and $\text{NaNO}_3\text{--MgO_B}$ samples were placed in a thermogravimetric analyser (TGA) and heated to 330°C (heating rate of $10^\circ\text{C min}^{-1}$) in a flow of N_2 (80 ml min^{-1}), followed by exposure to a flow of CO_2 (80 ml min^{-1}) for a given time (0.5 hour to 24 hours, *e.g.* $\text{NaNO}_3\text{--MgO_A}_{24\text{hours-}\text{CO}_2}$). For the duration of the experiment a purge flow of N_2 (25 ml min^{-1}) was used in the TGA. For subsequent *ex situ* analyses the sample is cooled down in CO_2 to 30°C (cooling rate of $10^\circ\text{C min}^{-1}$) to avoid the decomposition of MgCO_3 . To confirm the presence of salt

(NaNO_3) inside the grooves after the sample has been exposed to reaction conditions 3D X-ray computed tomography was applied.

3D visualization of NaNO_3 in the model system after CO_2 capture

To visualize and quantify the volume of NaNO_3 in the grooves of the model samples after CO_2 capture we turned to X-ray micro computed tomography (μCT), Fig. 2. A 3D render of the $\text{NaNO}_3\text{--MgO_B}$ system after 5 hours of exposure to CO_2 at 330°C , $\text{NaNO}_3\text{--MgO_B}_{5\text{hours-}\text{CO}_2}$, is shown in Fig. 2a. From the 3D render, it is clear that NaNO_3 no longer fills the entire volume of the groove, thus confirming a volumetric loss of NaNO_3 during carbonation. Moreover, the surface of the remaining volume of NaNO_3 forms a concave meniscus, which is an indication that the molecules of the liquid (molten NaNO_3) show stronger adhesion to the wall material (MgO) than to each other. A quantification of the volumetric NaNO_3 loss was performed by segmentation of MgO and NaNO_3 using their X-ray contrast. The volume fraction of NaNO_3 inside the groove is calculated by

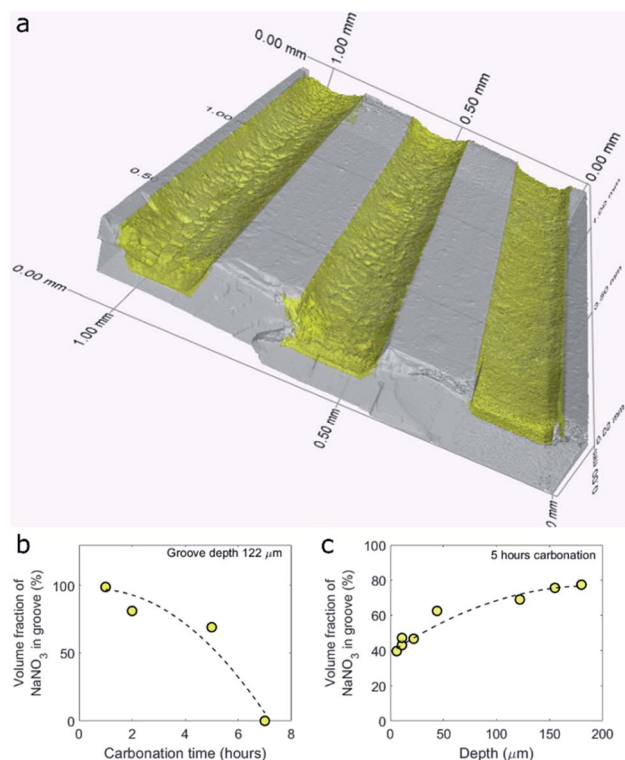


Fig. 2 Quantification of the volume fraction of NaNO_3 in the grooves of a $\text{MgO}(100)$ single crystal after carbonation using 3D X-ray micro computed tomography. (a) 3D render of three grooves in the NaNO_3 filled MgO sample ($\text{NaNO}_3\text{--MgO_B}$, groove depths of $d_{\text{grooves}} = 84, 44, 22 \mu\text{m}$) showing a volumetric loss of NaNO_3 after 5 hours of carbonation at 330°C in a CO_2 rich atmosphere (CO_2 flow of 80 ml min^{-1} with a purge flow of N_2 25 ml min^{-1}) *i.e.* $\text{NaNO}_3\text{--MgO_B}_{5\text{hours-}\text{CO}_2}$. Volume fraction of NaNO_3 in the grooves as a function of (b) carbonation time (groove with a depth of $122 \mu\text{m}$) and (c) volume fraction as function of groove depth after 5 hours of carbonation at 330°C in CO_2 . Second order polynomial fits are plotted as dashed lines.



summing up the number of voxels occupied by NaNO_3 and dividing it by the total number of voxels inside the groove. MgCO_3 and NaNO_3 have a similar X-ray contrast, which hindered differentiation of these two materials. Therefore, the volume of MgCO_3 is included in the volume of NaNO_3 , however it has a negligible contribution as the volume of MgCO_3 is significantly smaller than that of NaNO_3 . Fig. 2b and c plot the volume fraction of NaNO_3 in the groove as a function of, respectively, time and depth for the sample $\text{NaNO}_3\text{-MgO}_\text{B}$. Our results plotted in Fig. 2b show that the loss of NaNO_3 during carbonation accelerates (volume fraction of NaNO_3 is 100% for the as-prepared sample and decreases to 99 vol% after 1 hour, while after 7 hours of carbonation there is 0 vol% NaNO_3 in the groove of a depth of 122 μm). The accelerated loss is further evident through a second order polynomial fit to the data, as shown by the dashed line in Fig. 2b. Considering a fixed carbonation time of 5 hours, we observe that in shallower grooves the volume fraction of NaNO_3 is lower compared to deeper grooves, pointing to a faster volumetric loss of NaNO_3 in shallower grooves (Fig. 2c). The experiments are carried out at 330 $^\circ\text{C}$ (below the boiling point of NaNO_3 of 380 $^\circ\text{C}$) and the loss of NaNO_3 is ascribed to its evaporation (the vapor pressure of NaNO_3 at 330 $^\circ\text{C}$ is 3 mPa).²² Raman micro-spectroscopy of the NaNO_3 -filled grooves revealed that NaNO_3 did not change its phase during carbonation (where evaporation has occurred).

The accelerated loss of NaNO_3 as function of time and the faster loss of NaNO_3 in shallower grooves is very likely due to a higher surface to volume ratio in such configurations leading in turn to a higher rate of evaporation per volume NaNO_3 .^{23,24} The loss of the alkali metal salt promoter has also been observed in conventional powder samples. For example, Chen *et al.* observed that the mass ratio (measured by inductively coupled plasma – optical emission spectrometry ICP-OES) of alkali metal ions (*i.e.*, Li^+ , K^+ , Na^+) to Mg^{2+} decreased during cycling and was also attributed to the evaporation of the alkali metal salt.²¹ The faster loss of NaNO_3 in the model systems used here when compared to powder samples²¹ is very likely due to the high surface to volume ratio of the promoter in our model systems and larger capillary forces in the powder sample.²⁵ After having established a loss of NaNO_3 with carbonation time, we focus in the following on elucidating the role of NaNO_3 in accelerating the rate of MgCO_3 formation. To this end, we characterized in more detail the MgCO_3 formed in samples that have been exposed to CO_2 (76 vol%) for 5 hours or less, as the samples that were exposed for longer carbonation times had lost most of the NaNO_3 .

Identifying the location of MgCO_3 growth in the $\text{NaNO}_3\text{-MgO}$ model system

The location of MgCO_3 formed in the $\text{NaNO}_3\text{-MgO}$ model systems after their exposure to CO_2 is identified by Raman micro-spectroscopy, SEM energy dispersive X-ray spectroscopy (EDX), and plasma FIB-SEM EDX. The Raman spectra of two locations and EDX maps of a mechanically cleaved cross-section of one of the grooves in the $\text{NaNO}_3\text{-MgO}_\text{A5hours-}\text{CO}_2$ sample are provided in Fig. 3. Fig. 3a illustrates the spots in which Raman

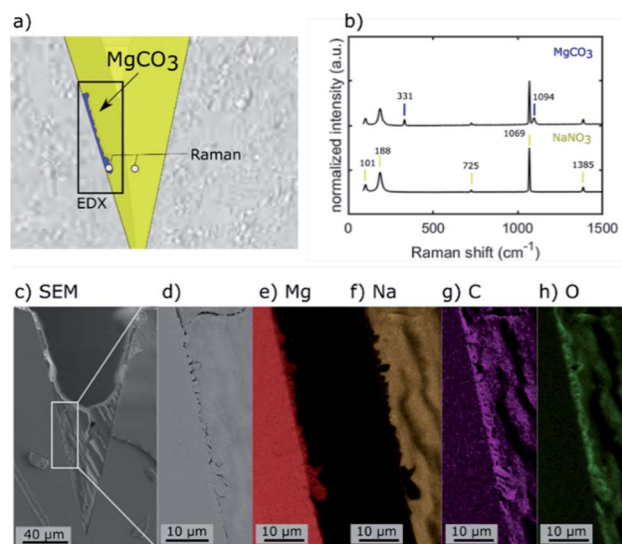


Fig. 3 EDX analysis and Raman micro-spectroscopy of a NaNO_3 filled groove ($\text{NaNO}_3\text{-MgO}_\text{A5hours-}\text{CO}_2$) after its exposure to CO_2 for 5 hours using a mechanically cleaved cross-section. (a) Illustration showing the location of the region used for EDX analysis and the two spots at which Raman spectra were acquired. (b) Raman spectra acquired at the two spots indicated in (a), *i.e.* inside the NaNO_3 promoter and at the wall of the groove where MgCO_3 was formed. (c) SEM image showing the entire cross-section including the NaNO_3 remaining at the bottom of the groove. (d–h) magnified SEM image and EDX elemental maps of Mg, Na, C, and O of the region highlighted in (a).

spectra were collected (spot size of *ca.* 0.6–1.8 μm) and the area used for EDX analysis. In the illustration, the phases MgO , MgCO_3 , NaNO_3 are highlighted in grey, blue and yellow colours, respectively, based on Raman spectra and EDX analysis. The Raman spectrum collected in a location in which NaNO_3 is present (colored yellow in Fig. 3a), shows bands at 101, 186, 724, 1067 and 1385 cm^{-1} that are characteristic of NO_3^- in NaNO_3 , Fig. 3b.^{15,26–29} The most intense band at 1067 cm^{-1} is attributed to symmetric stretching vibrations, while the bands at 101 cm^{-1} , 186 cm^{-1} , 724 cm^{-1} and 1385 cm^{-1} are due to asymmetric stretching vibrations of NO_3^- .²⁹ A representative spectrum acquired close to the wall of the groove (blue coloured region in Fig. 3a) exhibit bands associated with NO_3^- and two additional bands that are due to MgCO_3 .^{30,31} These additional Raman bands at 740 cm^{-1} and 1094 cm^{-1} are assigned to bending and symmetric stretching vibrations of CO_3^{2-} , respectively.^{15,30,31} Bands due to NaNO_3 are observed in the spectrum acquired in the (blue) region that has been assigned to MgCO_3 because the size of the MgCO_3 particle (width *ca.* 1–2 μm) is of approximately the same size as the laser spot and within the lateral precision of the sample stage. *Ex situ* Raman micro-spectroscopy of samples that have been exposed to varying carbonation times showed no noticeable phase change of NaNO_3 with carbonation time, Fig. S4,[†] confirming the phase stability of NaNO_3 under the conditions investigated here. The region of the cross-section used for EDX analysis is shown in the overview SEM image in Fig. 3c and with a higher magnification in Fig. 3d. The respective EDX elemental maps are given in



Fig. 3e–h. Comparing the magnified SEM image (Fig. 3d) with the elemental maps, it is clear that the structure observed at the wall of the groove contains Mg, C, O, while Na is absent, providing further evidence that the particle structure formed at the wall of the groove is indeed composed of MgCO_3 , in agreement with Raman micro-spectroscopy analysis.

Subsequently we used plasma FIB-SEM to obtain a smooth cross-section of a groove allowing for high quality stacks of SEM images of cross-sections through a groove (ca. $300\ \mu\text{m} \times 200\ \mu\text{m}$). This is shown schematically in Fig. 4a and b. A series of SEM micrographs taken after different times of plasma FIB milling along the length of the grooves are shown in Fig. 4c–f. Note that slice #1, shown in Fig. 4c, is at the same location as Fig. 3d (lower magnification) and the blue colour is used to visually ease the identification of the location of MgCO_3 . In the ESI S5,† we demonstrate how we use EDX analysis (Na, Mg, O) to identify the location of MgCO_3 and use this information to colour the SEM images in Fig. 4 with blue to highlight the structures that are composed of MgCO_3 . Three additional slices were milled by plasma FIB to provide 3D insight into the structure and location of MgCO_3 . Importantly, these additional FIB cuts demonstrate that (i) MgCO_3 grows at the NaNO_3/MgO interface, *i.e.* at the wall of the groove, and (ii) MgCO_3 grows both close, but also far away from the triple phase boundary (TPB). These observations are in agreement with earlier reports indicating that MgCO_3 grows at the buried NaNO_3/MgO interface.^{15,16} Indeed, our results establish that the TPB is not the

primary location for MgCO_3 nucleation and growth, as we do not see a higher fraction of MgCO_3 particles at the TPB compared to other locations of the NaNO_3/MgO interface. Additional analysis by SEM provides more evidence that MgCO_3 nucleates and grows both close and far away from the TPB (*vide infra*).

Morphology and location of MgCO_3 growth in the NaNO_3 – MgO model system

We gained further insight into the morphology and location of formation of MgCO_3 that is formed during carbonation by SEM (Fig. 5 and S6–S8†). Prior to the morphological analysis, the sample was rinsed in water for 1 minute to remove NaNO_3 exposing the MgCO_3 grown at the bottom of the grooves (NaNO_3 – MgO – $\text{B}_{x\text{hours}}\text{CO}_2$ where the subscript x refer to carbonation time).^{9,15} Representative examples of MgCO_3

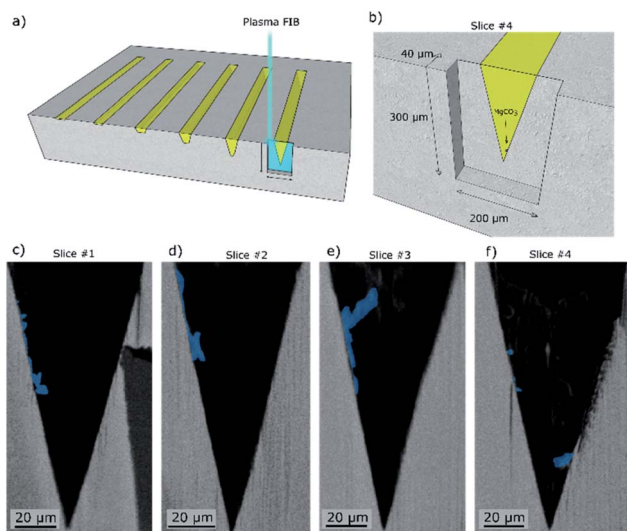


Fig. 4 Scanning electron micrographs of cross-sections obtained by plasma focused ion beam (FIB) milling taken at four different distances within the groove length (mechanically cleaved followed by broad ion beam (BIB) cross-section polishing). (a) The turquoise box marks the region of the model structure that was FIB milled. (b) Close up showing the location of slice #4 given in (c). (c–f) Series of cross-sectional SEM images whereby each slice is taken at a specific distance from the mechanical cleaved cross section of the sample NaNO_3 – MgO – $\text{A}_{5\text{hours}}\text{CO}_2$. The MgCO_3 phase is highlighted in blue for better visibility based on EDX analysis (ESI Fig. S2†). Slices #1–4 were taken at distances of ca. 0 μm , 5 μm , 10 μm and 40 μm from the mechanically cleaved surface, respectively.

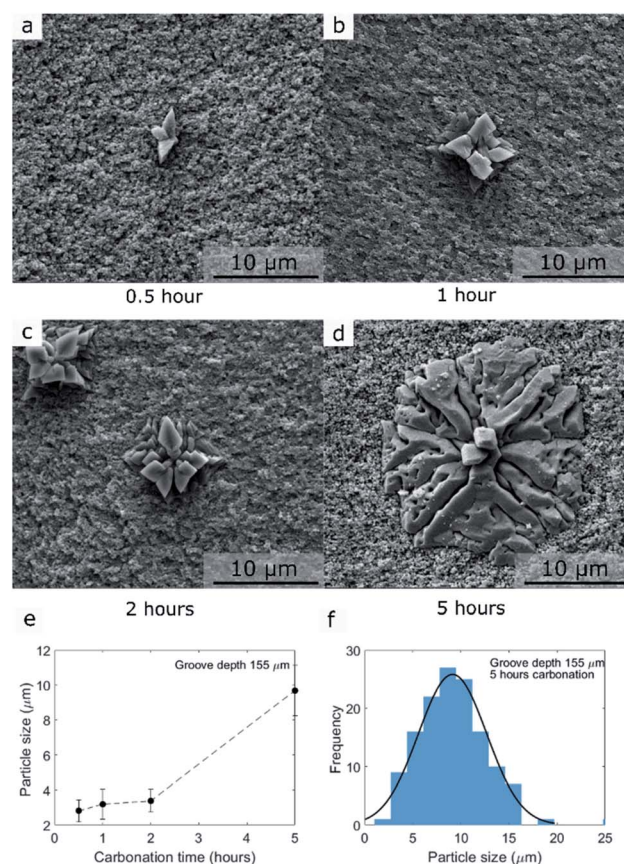


Fig. 5 Growth of MgCO_3 crystals with time when exposed to CO_2 at $330\ ^\circ\text{C}$ (sample NaNO_3 – MgO – $\text{B}_{x\text{hours}}\text{CO}_2$ where the subscript x corresponds to the carbonation time ranging between 0.5 hour and 5 hours). Prior to imaging/analysis the samples are rinsed in H_2O to remove NaNO_3 . (a–d) SEM images taken at the bottom of the MgO groove (groove depth $44\ \mu\text{m}$) after, respectively, 0.5 hour, 1 hour, 2 hours and 5 hours of exposure to CO_2 . (e) Mean particle size of MgCO_3 formed on the bottom of the grooves of depth $155\ \mu\text{m}$ as a function of carbonation time (error bars show the standard deviation of the measured particle diameter based on more than 100 particles per data point). (f) Exemplary particle size distribution in the groove of depth $155\ \mu\text{m}$ after 5 hours of carbonation (normal distribution function was used for fitting).



particles grown after 0.5, 1, 2, and 5 hours of carbonation (groove with a depth of $d_{\text{groove}} = 44 \mu\text{m}$) are shown in Fig. 5a–d. Additionally, an overview of the MgCO_3 particles grown after 5 hours at the bottom of deep and shallow grooves are shown in Fig. S6–S7.†

The mean particle size of MgCO_3 as a function of carbonation time (groove depth $44 \mu\text{m}$, $\text{NaNO}_3\text{-MgO}_{\text{B}_{x\text{hours-CO}_2}}$, $x = 0.5, 1, 2, 5$ hours) is plotted in Fig. 5e and the particle size distribution after 5 hours of carbonation at 330°C in CO_2 is given in Fig. 5f (groove depth $44 \mu\text{m}$, $\text{NaNO}_3\text{-MgO}_{\text{B}_{5\text{hours-CO}_2}}$). The number of particles (MgCO_3 particles as those observed in Fig. 5a–d are counted as one particle) is plotted as a function of groove depth (at the flat bottom) and carbonation time in Fig. S8.† Notice, only particles located at the flat bottom of the grooves in MgO_{B} are counted and since the bottom area is smaller in deeper grooves, the number of particles is normalized by the area of the bottom of the grooves. The CO_2 capture performance of AMS-promoted MgO powder samples can be quantified for example by its weight change in a TGA experiment, however, the weight changes (per gram of sample) in the model system are too small to be detected. To quantify the amount of absorbed CO_2 , instead we determined the fraction of the MgO surface (at the bottom of the groove) that is covered by MgCO_3 in Fig. S7† and the volume of MgCO_3 formed by profilometry below.

The examples of the MgCO_3 particles presented in Fig. 5 and S6–S7† show that MgCO_3 grows as individual crystals/particles and in some cases the individual crystals/particles have merged to form larger agglomerates covering a large fraction of the surface of MgO , Fig. S6.† The MgCO_3 particle grown after 0.5 hour of carbonation, Fig. 5, has a diameter of approximately $3 \mu\text{m}$ and consist of three smaller crystallites. Increasing the carbonation time to 5 hours leads to an increasing number of small crystallites, but also the further growth of existing crystallites, Fig. 5b–d. Overall, the shape of the individual particles formed in our model systems is very similar to the 2D MgCO_3 islands formed on $\text{MgO}(100)$ promoted with NaNO_3 .¹⁵ To obtain a full 3D representation of the formed MgCO_3 crystal, we performed additional focused ion beam (FIB) SEM tomography measurement of MgCO_3 grown on $\text{MgO}(100)$ single crystals promoted with NaNO_3 after 5 hours of CO_2 exposure (Fig. 6). The shape of the crystals/particles formed on the laser ablated surface, Fig. 5, point to a nucleation and crystal growth type process from a supersaturated solution of $[\text{Mg}^{2+} \dots \text{CO}_3^{2-}]$ in agreement with literature.^{10,14–16} While MgCO_3 forms through a nucleation and growth type process in both the laser ablated MgO sample, Fig. 5, and $\text{MgO}(100)$, Fig. 6, there are still some variations in the growth habit between these two systems. For example, each MgCO_3 particle grown on the ablated MgO surface is composed of a comparatively large number of small crystallites and there is a more extensive out-of-plane 3D growth (crystal thickness of up to $3 \mu\text{m}$, see below in Fig. 7) of the MgCO_3 crystals on the ablated MgO surface as compared to the MgCO_3 crystals grown on the surface of $\text{MgO}(100)$ single crystals (crystal thickness in the range $0.2\text{--}2 \mu\text{m}$), in agreement with our previous work.¹⁵ The mean particle size (in-plane) after 5 hours of exposure to CO_2 is $9 \pm 1 \mu\text{m}$ on the ablated surface in

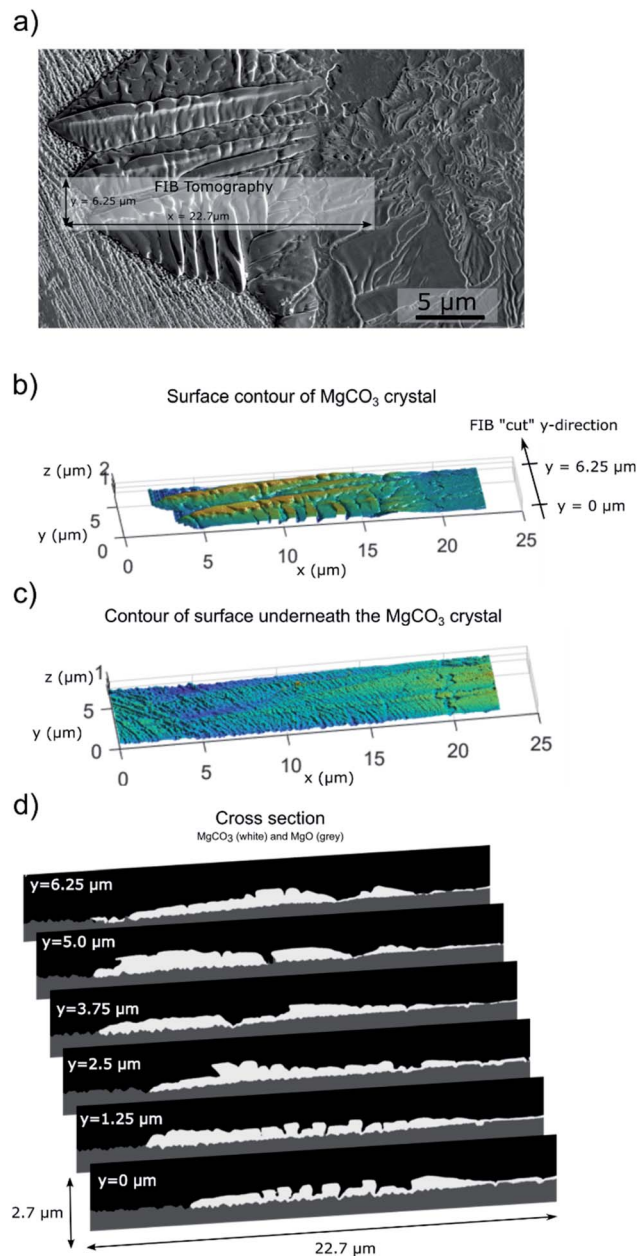


Fig. 6 FIB-SEM tomography of a MgCO_3 crystal grown on the surface of $\text{MgO}(100)$ promoted with NaNO_3 after 5 hours of exposure to CO_2 i.e. $\text{NaNO}_3\text{-MgO}(100)_{5\text{hours-CO}_2}$. Prior to the tomographic measurement the sample was rinsed in water. (a) SEM image of the MgCO_3 crystal grown on a $\text{MgO}(100)$ single crystal (the grey box shows the area that was used for the tomographic measurement; resolution in x, y, z is, respectively, 10 nm , 25 nm , and $\approx 10 \text{ nm}$). (b and c) Surface contours of MgCO_3 and MgO are determined by segmenting MgCO_3 and MgO through a combination of thresholding by grey-level (using the backscattered electron, BSE, signal) and a directional search for grey-level edges. (d) Segmentation of MgCO_3 and MgO in a cross-section (window size $[x,z] = 22.7 \times 2.7 \mu\text{m}$) along the y -direction. Each cross section is taken at a y -spacing of 25 nm and is shown at selected positions, i.e. $y = 0, 1.25, 2.5, 3.75, 5$, and $6.25 \mu\text{m}$.

comparison to a size of $10\text{--}50 \mu\text{m}$ on the $\text{MgO}(100)$ single crystal surface. The morphology of the MgCO_3 formed on the ablated MgO surface can be described as “radiating dendrites” in



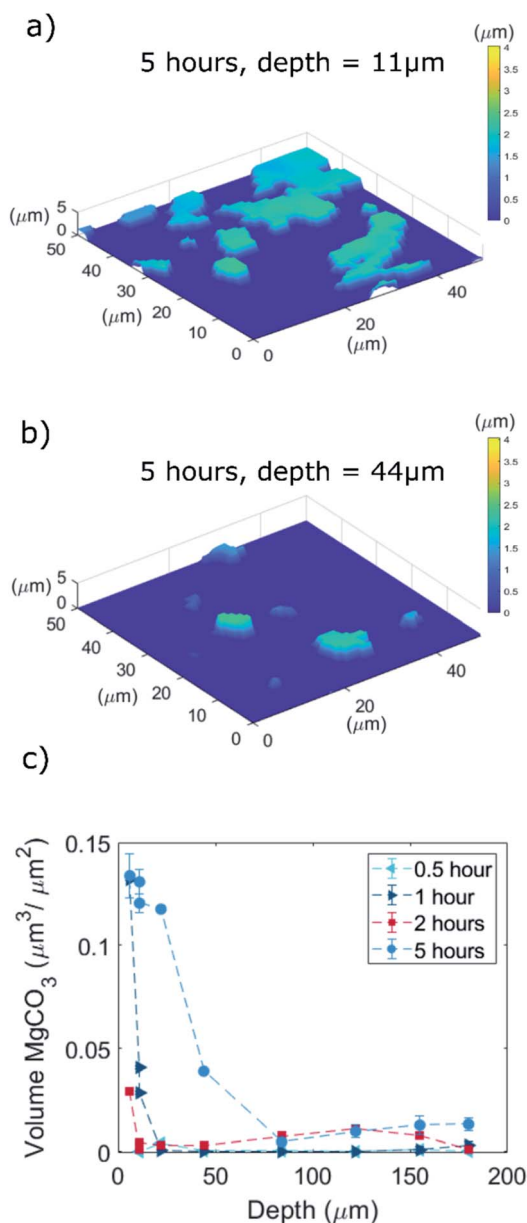


Fig. 7 Quantification of the volume of the MgCO₃ crystals by 3D profilometry measurements after removal of NaNO₃ by rinsing with H₂O. The volume is calculated by the sum of “voxels” of MgCO₃, *i.e.* the voxels that are at a height $z > 0$ μm with respect to the flat MgO surface at the bottom of the groove ($z = 0$ μm, roughness subtracted) multiplied by the dimension of the pixel in the xy direction (0.69×0.69 μm²). As the area at the bottom of a groove is smaller in deeper grooves, the MgCO₃ volume is normalized by the area of the bottom part of the groove. Note that the optical profile measurements rely on the reflection of light at the surface. Hence, only MgCO₃ grown at the bottom of the groove can be quantified, as the steep angle of the groove wall with respect to the incoming light minimizes reflection, which hinders quantification of the volume of MgCO₃ grown on the walls of the groove. (a and b) MgCO₃ formation after 5 hours of exposure to CO₂ in grooves with a depth of 11 μm and 44 μm, respectively. (c) Total volume of MgCO₃ crystals formed at the bottom of the grooves normalized by the area of the bottom of the groove as a function of the depth of the groove ($d_{\text{groove}} = 6, 11, 11, 22, 44, 84, 122, 155, 180$ μm) and carbonation time (0.5, 1, 2, 5 hours).

contrast to the “sector plate” morphology on MgO(100). To rationalize the differences in morphology of the MgCO₃ formed on these two model systems it is worth looking at the growth habits of ice crystals and ice analog crystals. Their growth habits have been mapped with respect to the level of supersaturation. For example, the crystal growth of Na₂SiF₆ from an aqueous solution *e.g.* can be induced by evaporation of the solution, whereby the supersaturation level is controlled by the rate of evaporation.²⁵ Under such conditions, sodium fluorosilicate crystals exhibit a “sector plate” morphology for lower levels of supersaturation while when increasing the degree of supersaturation “radiating dendrite” morphologies are observed. Assuming that there is a similar link between the degree of supersaturation and the growth habit for MgCO₃, we can infer that the laser ablated MgO surface provides an environment with a higher supersaturation level (radiating dendrite morphology with a larger number of small crystals) compared to a flat MgO(100) surface (sector plate morphology with a few large crystallites). The higher level of supersaturation of [Mg²⁺...CO₃²⁻] ionic pairs is likely a result of the more defective nature of the laser ablated surface promoting in turn the dissolution of MgO, yielding [Mg²⁺...O²⁻] ionic pairs which are the precursors to carbonate ionic pairs, as dissolution preferentially occurs on surface defects.³²

As described above, the locations of MgCO₃ formation are found both close and far away from the TPB. Indeed, we observe a homogenous distribution of MgCO₃ particles at the NaNO₃/MgO interface, Fig. S7,† with no preferential growth at the TPB. This observation is in agreement with the location of MgCO₃ particles seen in cross-sections of the grooves (Fig. 4). In addition, Fig. S6† shows that the number of MgCO₃ particles per surface area of MgO is independent of depth and time (note we count the structures visualized in Fig. 5a–d that comprise several smaller crystallites as one particle). For example, on average *ca.* 2000 MgCO₃ particles are found per mm² MgO in grooves with a depth of 11 μm. The same number of MgCO₃ particles per surface area MgO were also counted in grooves with a depth of 180 μm (Fig. S6a†). Assuming that each particle arises from a single nucleation event, these numbers confirm that MgCO₃ nucleation occurs with the same frequency under a thin and thick coating of NaNO on MgO, *i.e.*, relatively close and rather far away from the TPB. Since the morphology of the MgCO₃ crystals indicate crystal growth from a supersaturated solution and we observe a density of nucleation sites that is independent of time and depth we can conclude that the critical level of supersaturation that is required for the formation crystalline magnesium carbonate is reached in both the shallow and deep grooves (at least locally and within the timeframe studied here). To summarize, our results show that the location of MgCO₃ nucleation is at the NaNO₃/MgO interface and the density of nucleation sites is independent of the groove depth (*i.e.* the height/thickness of the promoter covering MgO). In other words, for the groove depths studied here the dissolution and diffusion of CO₂ to the reaction interface is not rate limiting for the nucleation step.

Lastly, we explored the volumetric growth of the MgCO₃ crystals in more detail and as a function of time and the



thickness of the NaNO_3 coating to assess whether diffusion of CO_2 through the promoter is rate limiting during the growth step.

3D visualization and quantification of the volume of MgCO_3 formed

To visualize and quantify the volume of the magnesium carbonate formed through CO_2 absorption at the bottom of the grooves in the NaNO_3 - MgO _B model system, we used 3D optical profilometry (Fig. 7). The MgCO_3 formed appeared at heights with $z > 0 \mu\text{m}$ with respect to the originally flat MgO surface ($z = 0 \mu\text{m}$). Fig. 6a and b visualize a series of MgCO_3 particles at the bottom of two different grooves with depths of, respectively, 11 and 44 μm (the samples were exposed to CO_2 for 5 hours and rinsed with water prior to the measurements, NaNO_3 - MgO _B-5hours- CO_2). We observe that in the first 2 hours of carbonation the MgCO_3 structures grow with equal rates in all three dimensions *i.e.* after 2 hours of carbonation the particles have a width and thickness of 2 μm . Subsequently, MgCO_3 grows largely in a 2 dimensional fashion, *i.e.* parallel to the MgO plane (*i.e.* after 5 hours of carbonation MgCO_3 has a thickness of *ca.* 2 μm and lateral dimension of 10 μm) leading to the formation of “2D islands” that in some cases merge to form larger agglomerates. This observation is in agreement with a previous study that reported the formation of 2D islands of MgCO_3 (thickness in the range of 0.2–2 μm and lateral dimension in the range 10–50 μm) after 5 hours of carbonation of a NaNO_3 -promoted single crystals of MgO (100).¹⁵ From our profilometry results acquired at the bottom of various grooves, it is clear that shallower grooves (*e.g.* depth of 11 μm) contain MgCO_3 particles that have a larger volume (when normalized by the available surface area of MgO at the bottom of the groove) than those formed in deeper grooves (*e.g.* of depth 44 μm). This is in agreement with our SEM results (Fig. S9†) revealing that the bottom of shallow grooves are almost fully covered by MgCO_3 whereas the bottom of deeper grooves shows a significantly lower coverage of MgCO_3 . Thus, a thinner coating of NaNO_3 facilitates the further growth of MgCO_3 . This is in contrast to the observations made for the nucleation step which was found to be independent of the coating thickness.

The volume (per unit area of the bottom section of the groove) of the MgCO_3 particles formed at the bottom of grooves as function of the groove depth after exposure to CO_2 for 0.5, 1, 2, and 5 hours is shown in Fig. 7c. Considering the sample that has been exposed to CO_2 for 5 hours, the MgCO_3 formed at the bottom of the shallow groove ($d_{\text{groove}} = 6 \mu\text{m}$) has a total volume of 0.13 $\mu\text{m}^3 \mu\text{m}^{-2}$ compared to a total MgCO_3 volume of 0.013 $\mu\text{m}^3 \mu\text{m}^{-2}$, *i.e.* 10 times lower, in the deepest groove ($d_{\text{groove}} = 180 \mu\text{m}$). The same trend is apparent for the samples that have been exposed to CO_2 for either 1 or 2 hours, while no apparent trend between MgCO_3 volume and groove depths is observed for a CO_2 exposure of 0.5 hour, presumably because at these short carbonation times crystal growth is still limited (instead nucleation dominates) and CO_2 diffusion has limited effects on the nucleation step. To summarize, in Fig. 7c we observe a clear trend of an accelerated growth of MgCO_3 in shallow grooves

compared to deep grooves, which is attributed to a shorter diffusion path length of CO_2 to the reaction interface in such systems, yielding in turn a higher density of ionic pairs of magnesium carbonate. It is conceivable that the faster evaporation rate of NaNO_3 as observed in shallower grooves also contributes to a faster precipitation of MgCO_3 .

Experimental

Laser ablation of grooves in MgO

MgO single crystals (MgO (100), Alineason, $\geq 99.95\%$ 10 mm \times 10 mm \times 0.5 mm) were used as purchased. The fabrication of grooves of varying depths in the MgO single crystals was carried out by ultra-short pulse (USP) laser ablation generating a defined geometry of high surface smoothness. A frequency-doubled Amphos 200 laser source of 515 nm wavelength, 800 fs pulse duration, and a power of up to 120 W was used. The laser beam was set to circular polarization using a quarter-waveplate and coupled into a galvo scanner, where the MgO crystal was placed on a high-precision xyz-stage. For all samples we used a 2.5D strategy *i.e.* removal of material layer-by-layer, see ESI Fig. S1† for illustration of the ablation process. For one ablated layer, the laser ablates the surface in parallel lines with a line distance of $l_b = 5 \mu\text{m}$. In the next layer, the sample was rotated by $\gamma_{\text{layer}} = 90^\circ$ thus ablates perpendicular to the previous lines and achieving a cross hatching pattern. To reach the desired groove depth the number of ablated layers was adjusted. For MgO _A, the laser pulse repetition rate was set to $f_{\text{rep}} = 400 \text{ kHz}$, the laser scan speed was $v_s = 400 \text{ mm s}^{-1}$ and an average power of 1 W used at a focal diameter of $d_{\text{focus}} = 9 \mu\text{m}$. To avoid re-deposition of ablated MgO , a flow of pressurized air mitigated the accumulation of debris during ablation. A subsequent laser cleaning step removed re-deposited MgO on the walls by ablation of the grooves once more with 0.3 W average power. Finally, the samples were cleaned in ethanol by ultra-sonication for 10 minutes. For the MgO _B samples we used a comparable system using a Trumpf TruMicro 5270 laser ($f_{\text{rep}} = 800 \text{ fs}$ pulse duration). The ablation process was slightly modified by using a larger focal diameter of $d_{\text{focus}} = 16 \mu\text{m}$ and using a laser pulse repetition rate of $f_{\text{rep}} = 600 \text{ kHz}$ and a laser scan speed of $v_s = 500 \text{ mm s}^{-1}$ (2 W of average power). Further details on the laser ablation process and its optimization for single crystal MgO (100), we refer to ref. 33.

Coating laser-ablated MgO (100) with NaNO_3 and carbonation experiments

To complete the preparation of the NaNO_3 - MgO model system, the laser-ablated single crystal MgO samples containing grooves of different depths were filled with the promoter NaNO_3 . To fill the grooves, approximately 1 g of crystalline sodium nitrate (NaNO_3 , Sigma-Aldrich, $\geq 99.5\%$) powder was placed as-received in an Al_2O_3 crucible with a diameter of 10 mm. The MgO crystal was placed with the grooves facing down towards the loosely packed NaNO_3 powder. The crucible with the MgO crystal was placed for 2 minutes on a hot plate (surface temperature of 375 $^\circ\text{C}$) and subsequently cooled down to 25 $^\circ\text{C}$ at ambient



conditions. This procedure yielded a sample with crystalline NaNO_3 filling the grooves of the MgO single crystal with some excess salt. To remove the excess promoter NaNO_3 , the sample was polished with sandpaper (2601 Sianor J, Grit 410, Sia Abrasives). For carbonation, the sample is placed into a thermogravimetric analyzer (TGA) and exposed to a flow of CO_2 (80 ml min^{-1} was used with a purge flow of N_2 25 ml min^{-1}) at 330 $^\circ\text{C}$ for a duration between 30 minutes to 24 hours with heating and cooling rates of 10 $^\circ\text{C min}^{-1}$.

3D X-ray micro computed tomography

For X-ray micro computed tomography (CT) measurements, the NaNO_3 - MgO groove samples (5 mm \times 5 mm \times 0.5 mm) were cleaved mechanically into smaller pieces (1–2 mm \times 10 mm \times 0.5 mm) to reach a high resolution. CT measurements were carried out using an Easy Tom XL from RX Solutions with the X-ray tube operating at 80 kV and 30 μA current. The CT scans were performed using a Varian PaxScan 2520DX detector. The voxel size of the scans was *ca.* 1.5 μm .

Raman micro spectroscopy

Raman spectra were acquired with a Thermo Scientific Instrument equipped with a 455 nm laser and a spot size of 1.8 μm and 0.6 μm for a 10- and 100-fold magnification, respectively. Spectra were collected in the range of 100–3500 cm^{-1} with a spectral resolution of 0.96 cm^{-1} and a laser power of 3 mW. Each spectrum consisted of five repetitions with a total integration time of 25 seconds.

Plasma FIB-SEM and SEM

Large cross-sections of the MgO single crystal containing grooves (*ca.* 300 μm \times 200 μm) for scanning electron microscopy (SEM) and energy dispersive X-ray spectroscopy (EDX) were prepared through plasma focused ion beam (FIB) milling and acquired by a Tescan Fera3. The microstructure and particle size of the MgCO_3 product formed on the surface of MgO (after removal of NaNO_3) was characterized by SEM using a FEI Quanta 200F.

FIB-SEM tomography

3D FIB-SEM tomography of a MgCO_3 crystal grown on NaNO_3 -promoted MgO after 5 hours of exposure to CO_2 is performed on a FIB-SEM Helios 5 UX. The imaging resolution was 10 \times 25 \times 10 nm^3 . SEM images of the backscattered electrons (BSE) signal using the through the lens detector (TLD) were acquired. Prior to the tomographic measurement, a “T”-shaped fiducial marker was cut to enable alignment of the stack of images. For data analysis, registration was performed using the Stackreg plugin (<https://bigwww.epfl.ch/thevenaz/stackreg/>) for ImageJ. “Salt and pepper” noise in the SEM 3D image is removed using Matlab's medfilt3, which performs median filtering in three dimensions. We used a setting of medfilt(A,9,9,9), where each voxel in the 3D image “A” contains the median value of the 9 by-9-by-9 neighbourhood around the corresponding voxel in A. Subsequently, segmentation is performed using the BSE

signal based on a combination of thresholding using the grey-level and directional search for grey-level edges.

3D surface profiling

The topography of the surface of the bottom of the MgO grooves, after the removal of NaNO_3 , was measured using a Sensofar S Neox 3D vertical scanning interferometer. All measurements were acquired using a EPI 20X objective with a pixel size 0.128 μm \times 0.128 μm and a lateral resolution of 0.01 μm . The volume of the MgCO_3 particles formed at the flat bottom of the grooves (sample MgO_B) was determined by summing up the “voxels” of MgCO_3 . The voxels correspond to the height, z , with respect to the bottom of the MgO groove ($z = 0$), multiplied by the pixel size (0.69 μm \times 0.69 μm). The volume of MgCO_3 formed was determined on the entire bottom area of each groove and since the area of the bottom of a groove depends on the depth of the groove, the volume of MgCO_3 is normalized by the surveyed area.

Conclusion

In this work, we fabricated a model system of a MgO -based CO_2 sorbent, *i.e.* a $\text{MgO}(100)$ single crystal containing grooves of defined geometry that are filled with a molten salt promoter. These well-defined model structures allowed us to identify the location of MgCO_3 nucleation and growth, *i.e.* the (buried) NaNO_3/MgO interface or the triple phase boundary (TPB), extract indications of the prevailing level of supersaturation and assess the possibility of diffusive limitations to the nucleation and growth process. SEM image analysis demonstrates clearly that MgCO_3 crystals grow at the NaNO_3/MgO interface and not inside the melt. Importantly, there was no preference of MgCO_3 nucleation at the TPB compared to the buried NaNO_3/MgO interface. There is no observable CO_2 diffusion limitation on the nucleation step indicating that all grooves (deep and shallow) reach the critical supersaturation for nucleation within the first 30 minutes of carbonation.

Comparing the growth of crystalline MgCO_3 in shallow (6 μm) and deep (180 μm) grooves shows that the growth rate of MgCO_3 is approximately an order of magnitude higher in shallow grooves compared to that in deep grooves (after 5 hours of exposure to CO_2). We attribute this observation to the shorter diffusion path of CO_2 from the gas phase to the reaction interface indicating that the dissolution and transport of CO_2 is the rate-limiting step for the growth of MgCO_3 . However, it is conceivable that the increased rate of NaNO_3 evaporation in shallower grooves also contributes to a faster precipitation of MgCO_3 . In summary, our findings indicate that an effective MgO -based sorbent should contain a homogenous, conformal coating of an alkali metal salt promoter to increase the area of the promoter- MgO interface. To yield rapid MgCO_3 growth kinetics (*i.e.* a high rate of CO_2 uptake), the salt coating should be thin enough to avoid diffusive limitations and MgO should be highly porous (micro- to mesoporous) with subsequent coating (infiltration) as to maximize the interfacial contact between the salt and the oxide surface.



Conflicts of interest

There are no conflicts to declare.

Acknowledgements

This project has received funding from the European Research Council (ERC) under the European Union's Horizon 2020 research and innovation program grant agreement No. 819573 and from the Swiss National Science Foundation (SNSF, 200020_156015). The authors thank the Scientific Centre for Optical and Electron Microscopy (ScopeM) of ETH Zürich for providing access to electron microscopy. We further thank Prof. Konrad Wegener for access to a 3D surface profiling microscope, and Lukas Seeholzer for equipment support. We acknowledge the Philippe Thévenaz, Biomedical Imaging Group, Swiss Federal Institute of Technology Lausanne for the ImageJ plugin for the recursive alignment of images for FIB-SEM tomography.

References

- 1 M. T. Dunstan, F. Donat, A. H. Bork, C. P. Grey and C. R. Müller, *Chem. Rev.*, 2021, **121**, 12681–12745.
- 2 M. Haaf, R. Anantharaman, S. Roussanaly, J. Ströhle and B. Epple, *Resour., Conserv. Recycl.*, 2020, **162**, 104973.
- 3 D. P. Hanak, S. Michalski and V. Manovic, *Energy Convers. Manage.*, 2018, **177**, 428–452.
- 4 M. Bhagiyalakshmi, J. Y. Lee and H. T. Jang, *Int. J. Greenhouse Gas Control*, 2010, **4**, 51–56.
- 5 K. K. Han, Y. Zhou, W. G. Lin and J. H. Zhu, *Microporous Mesoporous Mater.*, 2013, **169**, 112–119.
- 6 W. Gao, T. Zhou and Q. Wang, *Chem. Eng. J.*, 2018, **336**, 710–720.
- 7 W. J. Liu, H. Jiang, K. Tian, Y. W. Ding and H. Q. Yu, *Environ. Sci. Technol.*, 2013, **47**, 9397–9403.
- 8 X. Zhao, G. Ji, W. Liu, X. He, E. J. Anthony and M. Zhao, *Chem. Eng. J.*, 2018, **332**, 216–226.
- 9 K. Zhang, X. S. Li, W. Z. Li, A. Rohatgi, Y. Duan, P. Singh, L. Li and D. L. King, *Adv. Mater. Interfaces*, 2014, **1**, 1–6.
- 10 T. Harada, F. Simeon, E. Z. Hamad and T. A. Hatton, *Chem. Mater.*, 2015, **27**, 1943–1949.
- 11 A. T. Vu, Y. Park, P. R. Jeon and C. H. Lee, *Chem. Eng. J.*, 2014, **258**, 254–264.
- 12 K. Zhang, X. S. Li, Y. Duan, D. L. King, P. Singh and L. Li, *Int. J. Greenhouse Gas Control*, 2013, **12**, 351–358.
- 13 W. Gao, J. Xiao, Q. Wang, S. Li, M. A. Vasiliades, L. Huang, Y. Gao, Q. Jiang, Y. Niu, B. Zhang, Y. Liu, H. He and A. M. Efstathiou, *Adv. Mater.*, 2022, **34**, 2106677.
- 14 H. Jeon, M. L. T. Triviño, S. Hwang, J. H. Moon, J. Yoo and J. G. Seo, *J. CO₂ Util.*, 2020, **39**, 101153.
- 15 A. H. Bork, M. Rekhtina, E. Willinger, P. Castro-Fernandez, J. Drnec, P. M. Abdala and C. R. Müller, *Proc. Natl. Acad. Sci.*, 2021, **118**, 26.
- 16 S. I. Jo, Y. I. An, K. Y. Kim, S. Y. Choi, J. S. Kwak, K. R. Oh and Y. U. Kwon, *Phys. Chem. Chem. Phys.*, 2017, **19**, 6224–6232.
- 17 G. J. Janz and N. P. Bansal, *J. Phys. Chem. Ref. Data*, 1982, **11**, 505–693.
- 18 H. Lee, M. L. T. Triviño, S. Hwang, S. H. Kwon, S. G. Lee, J. H. Moon, J. Yoo and J. G. Seo, *ACS Appl. Mater. Interfaces*, 2018, **10**, 2414–2422.
- 19 F. L. P. Veenstra, N. Ackerl, A. J. Martín and J. Pérez-Ramírez, *Chem*, 2020, **6**, 1707–1722.
- 20 N. Ackerl, A. H. Bork, R. Hauert, E. Müller and M. Rottmar, *Appl. Surf. Sci.*, 2021, **545**, 149020.
- 21 J. Chen, L. Duan, F. Donat and C. R. Müller, *ACS Sustainable Chem. Eng.*, 2021, **9**, 6659–6672.
- 22 V. I. Glazov, G. P. Dukhanin and M. K. Dkhaibe, *Russ. J. Appl. Chem.*, 2003, **76**, 1405–1407.
- 23 I. Langmuir, *Phys. Rev.*, 1918, **12**, 368.
- 24 F. Dalla Barba, J. Wang and F. Picano, *Phys. Fluids*, 2021, **33**, 1–5.
- 25 M. J. Krasinski and J. Prywer, *J. Cryst. Growth*, 2007, **303**, 105–109.
- 26 M. D. Fontana, K. Ben Mabrouk and T. H. Kauffmann, *4th IMEKO TC19 Symp. Environ. Instrum. Meas. 2013 Prot. Environ. Clim. Chang. Pollut. Control*, 2013, pp. 27–29.
- 27 H. J. Tong, J. P. Reid, J. L. Dong and Y. H. Zhang, *J. Phys. Chem. A*, 2010, **114**, 12237–12243.
- 28 J. Y. Yu, Y. Zhang, G. Zeng, C. M. Zheng, Y. Liu and Y. H. Zhang, *J. Phys. Chem. B*, 2012, **116**, 1642–1650.
- 29 D. L. Rousseau, R. E. Miller and G. E. Leroi, *J. Chem. Phys.*, 1968, **48**, 3409–3413.
- 30 P. Gillet, *Am. Mineral.*, 1993, **78**, 1328–1331.
- 31 Q. Williams, B. Collerson and E. Knittle, *Am. Mineral.*, 1992, **77**, 1158–1165.
- 32 J. A. Mejias, A. J. Berry, K. Refson and D. G. Fraser, *Chem. Phys. Lett.*, 1999, **314**, 558–563.
- 33 N. Ackerl, PhD Thesis, ETH Zurich, Zurich, Switzerland, 2020.

